SCIENTIFIC REP**O**RTS

OPEN

Single Walled BiI$_3$ Nanotubes Encapsulated within Carbon Nanotubes

Anumol Erumpukuthickal Ashokkumar[1], Andrey N. Enyashin[2,3] & Francis Leonard Deepak[1]

Inorganic nanotubes are morphological counterparts of carbon nanotubes (CNTs). Yet, only graphene-like BN layer has been readily organized into single walled nanotubes so far. In this study, we present a simple route to obtain inorganic single walled nanotubes - a novel ultrathin morphology for bismuth iodide (BiI$_3$), embedded within CNTs. The synthesis involves the capillary filling of BiI$_3$ into CNT, which acts as a nanotemplate, by annealing the BiI$_3$-CNT mixture above the melting point of BiI$_3$. Aberration corrected scanning/transmission electron microscopy is used in characterizing the novel morphology of BiI$_3$. A critical diameter which enables the formation of BiI$_3$ nanotubes, against BiI$_3$ nanorods is identified. The relative stability of these phases is investigated with the density functional theory calculations. Remarkably, the calculations reveal that the single walled BiI$_3$ nanotubes are semiconductors with a direct band gap, which remain stable even without the host CNTs.

Single walled nanotubes (SWNTs) of inorganic compounds akin to those of carbon are an outstanding set of nanomaterials that have attracted great attention for a variety of properties and applications[1–3]. Although the multi-walled counterparts are readily synthesized in the case of layered compounds including those of MoS$_2$, WS$_2$, etc. the synthesis of the SWNTs in the case of inorganic compounds poses a great challenge and a hurdle for investigating novel phenomena, properties and applications[4,5]. The formation thermodynamics of inorganic SWNTs is associated only to their high strain energies, not involving naturally any interlayer interaction. Hence, narrow SWNTs of inorganic compounds have been predicted to be less stable than their multi-walled counterparts[6,7]. This might explain the great difficulty, for example, in the synthesis of SWNTs of MoS$_2$ and WS$_2$, etc. However this challenge has been overcome recently with the synthesis of SWNTs of PbI$_2$ with the aid of CNTs which served as ideal templates for their formation[3]. Single layered metal halides of CeI$_3$, CeCl$_3$, TbCl$_3$ and ZnI$_2$ have also been synthesized by this approach[8]. The initial studies on opening up of carbon nanotubes and their encapsulation with metals and oxides were performed by Ajayan and Iijima as well as by Green and coworkers[9–11]. Dujardin *et al.* observed that the surface tension of materials play an important role in capillarity, with a low surface tension leading to wetting of CNT surface and capillary filling[12]. Subsequently, the hollow interior of CNTs was shown to provide a unique environment for the filling of molecules, compounds and meta-stable phases and serves as an ideal template for the growth of nanostructures with novel properties[13–16]. This unique feature of CNT has been exploited in the present study wherein the formation of BiI$_3$ SWNTs has been achieved starting from MWCNTs (multi-walled CNTs) as templates.

BiI$_3$ is a layered semiconducting material having a wide band gap reported to be 1.67 eV. A single layer BiI$_3$ is a sandwich-like structure with Bi^{3+} ions establishing six-fold coordination with I$^-$ ions. The BiI$_3$ layers are held together through weak van der Waals forces, allowing BiI$_3$ crystals to be cleaved readily along the [001] direction[17–19]. A schematic structural model of BiI$_3$ unit cell along with the unit cell parameters is shown in Fig. 1. The layered nature of BiI$_3$ is also shown. BiI$_3$, having high effective atomic number and high absorption coefficient, is an important material in radiation detection. Thus it has potential applications in room-temperature γ-ray detectors and X-ray digital imaging sensors[20,21]. Recently, appreciable interest has been directed to the optical properties of BiI$_3$ because of its strong intrinsic optical anisotropy and the potential for "defect-tolerant" charge

[1]Nanostructured Materials Group, Department of Advanced Electron Microscopy, Imaging and Spectroscopy, International Iberian Nanotechnology Laboratory (INL), Avenida Mestre Jose Veiga, Braga, 4715-330, Portugal. [2]Institute of Natural Sciences and Mathematics, Ural Federal University, Turgeneva Str., 4, 620083, Ekaterinburg, Russian Federation. [3]Institute of Solid State Chemistry, Ural Branch of Russian Academy of Sciences, Pervomayskaya Str., 91, 620990, Ekaterinburg, Russian Federation. Correspondence and requests for materials should be addressed to F.L.D. (email: leonard.francis@inl.int)
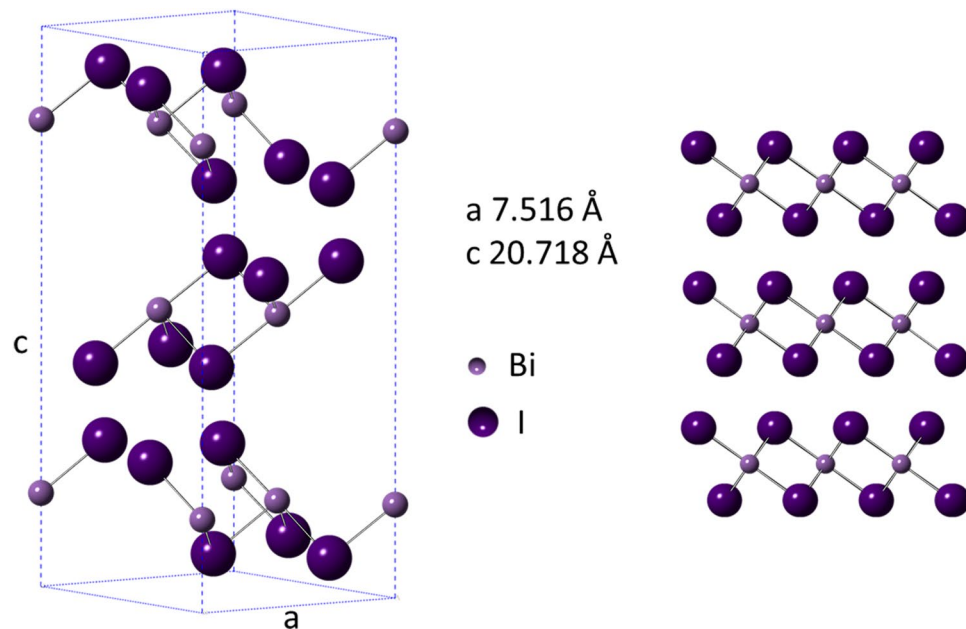
Figure 1. Structural model of rhombohedral BiI_3 showing the unit cell (left) and the crystal along (100) view direction showing the layered structure (right).

transport properties, making it a suitable candidate as thin-film photovoltaic absorber as well as acceptors in inorganic–organic solar cells[22].

Multi-walled core–shell $BiI_3@WS_2$ inorganic nanotubes (INT) were synthesized previously by employing the molten salt technique which basically involved the wetting and capillary filling of liquid BiI_3 into the INT template[23]. Nanotubes of mono elemental Bi have been reported earlier[24–26]. One-dimensional nanowires of Bi hosted within SWNTs have also been previously synthesized by heating solid bismuth nanoparticles with SWCNTs[27]. In the present study, the formation of single walled BiI_3 nanotubes encapsulated within CNT is reported for the first time; achieved by annealing the bulk powder of BiI_3 along with the host CNT at temperatures slightly above the melting point of BiI_3. Subsequently in-depth characterization of the morphology, structure and phase was carried out by aberration-corrected high-resolution transmission electron microscopy (AC-HRTEM) and high angle annular dark field scanning transmission electron microscopy (HAADF-STEM) imaging in combination with energy dispersive X-ray spectroscopy (EDX) and electron energy loss spectroscopy (EELS). A threshold diameter for the formation of the nanotubes in comparison to their counterparts - nanorods - was clearly established. In order to understand the formation peculiarities of these novel BiI_3 phases, density functional theory (DFT) calculations were carried out, to establish their relative stability and electronic properties.

Results and Discussions

Figure 2 shows the typical morphology of BiI_3 NT@CNT obtained after capillary filling method. In the HAADF-STEM image, BiI_3 is seen as the brighter region within the darker CNT region (with 8 walls) due to the Z dependence of the image contrast[28]. The BiI_3 nanotube walls appear particularly brighter in this image. The contrast due to the single walled nature of the BiI_3 is seen in the TEM image shown in Fig. 2b as well. The BiI_3 SWNT formed is single crystalline in nature, equivalent to a 2D sheet of BiI_3 wrapped into a cylinder as shown in Supplementary Fig. S1. The FFT of a region in Supplementary Fig. S1 is in agreement with the simulated diffraction pattern of the tube viewed along the [001] zone axis of the rhombohedral BiI_3 crystal (PDF Number: 00-007-0269), shown in Supplementary Fig. S1d.

STEM-EDX elemental mapping of the BiI_3 NT@CNT confirms the presence of Bi and I (Fig. 3a) and the quantification of the EDX spectrum reveals the elemental Bi:I ratio as 1:3, corresponding to BiI_3 (Fig. 3b, Supplementary Table S3). The EDX line profiles in Fig. 3c indicate a single walled tube with the highest intensity of Bi and I at the tube walls and decreased intensity towards the center. In addition to BiI_3 nanotubes, we observed BiI_3 nanorods within CNT. The STEM-EDX elemental maps on the BiI_3 nanorod@CNT (BiI_3 NR@CNT) show the distribution of Bi and I and the quantification of the EDX spectra established the 1:3 ratio of Bi:I as in BiI_3 (Supplementary Fig. S2). EELS measurement on the encapsulated nanorods show Bi $M_{4, 5}$ and I $M_{4, 5}$ edges, with edge onsets at 2604 eV and 628 eV, respectively, confirming the encapsulation of BiI_3 (Supplementary Fig. S2). Supplementary Figs S3 and S4 show the crystal orientation of BiI_3 nanorods in two different variants; [100] and [−111] of rhombohedral BiI_3.

In addition to single walled nanotubes and nanorods of BiI_3, there were nanotubes which appear to be partially filled. Figure 4a shows a $BiI_3@CNT$ where a single walled BiI_3 nanotube is observed within MWCNT as well as regions where the BiI_3 NT is filled resulting in a rod-like appearance. Figure 4b shows the HAADF intensity profiles across the tube at position 1 and 2 shown in inset Figure 4a. The analysis confirms that the BiI_3 NT is
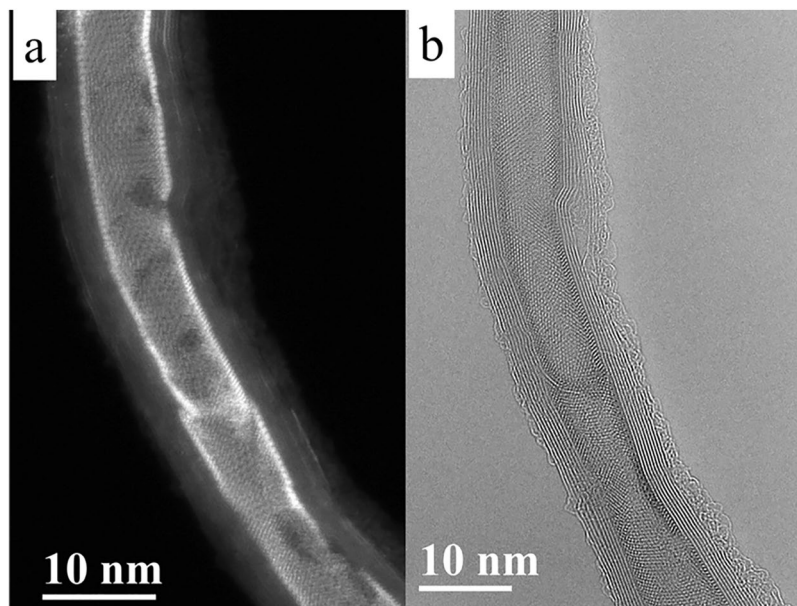
Figure 2. BiI_3 NT@CNT. (**a**) HAADF-STEM image and (**b**) AC-HRTEM image showing the encapsulation of BiI_3 as a single walled nanotube within CNT.
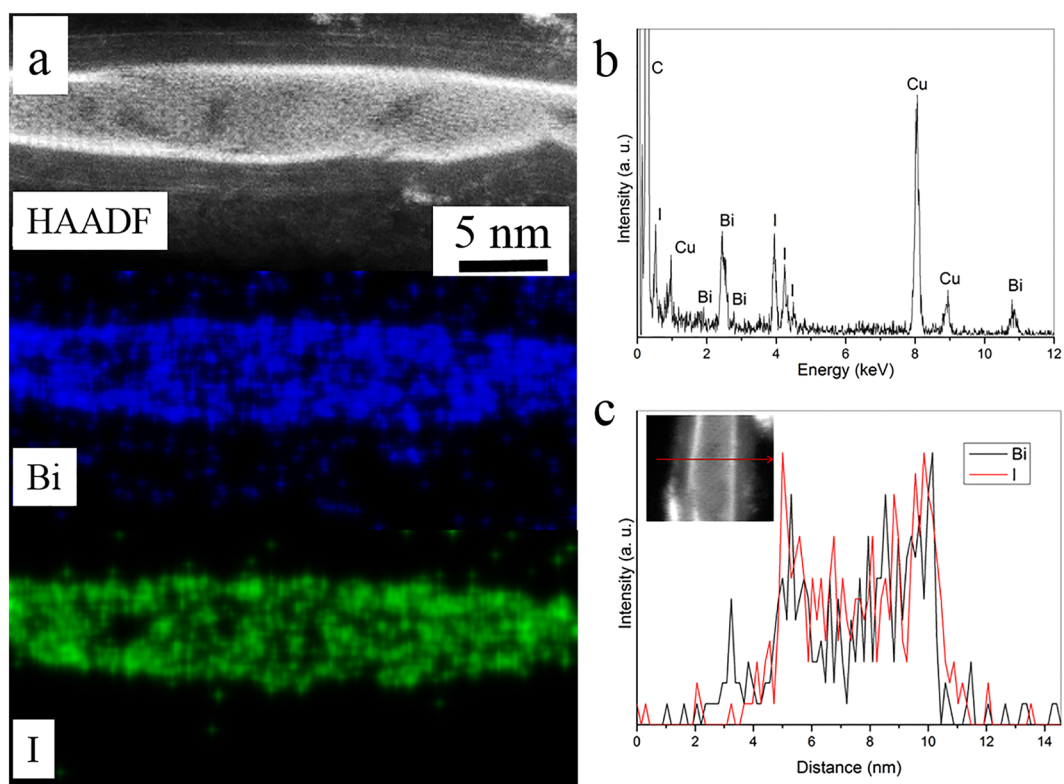

Figure 3. BiI_3 NT@CNT. (**a**) HAADF-STEM image and EDX elemental maps showing Bi and I. (**b**) EDX spectrum showing C, Bi, I peaks. (**c**) EDX line profile for Bi and I along the line across the BiI_3 NT@CNT shown in inset, confirming the tube morphology of BiI_3 within CNT.

present as single walled and filled, at positions 1 and 2, respectively. The (003) planes visible in the filled region shown in Fig. 4c, show an epitaxial relation with the (002) planes of the MWCNT template (Fig. 4d).

Low magnification images showing the encapsulation of BiI_3 as nanorods, nanotubes and partially filled nanotubes are shown in Fig. 5 and Supplementary Fig. S5. From the electron microscopy images, the yield of
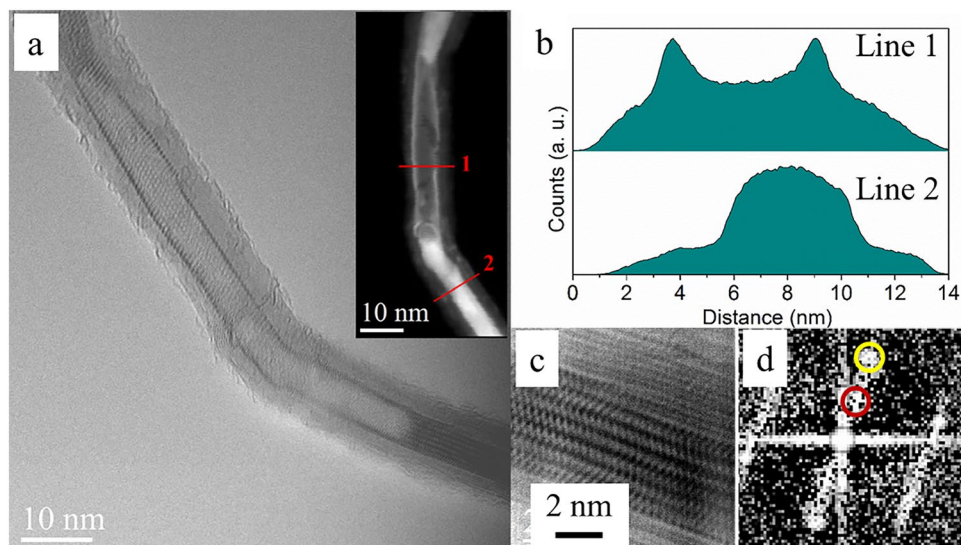
Figure 4. Partially filled BiI_3 NT@CNT. (**a**) HRTEM image (HAADF-STEM image as inset). (**b**) The intensity profile along line 1 and 2 in the inset showing the hollow BiI_3 NT@CNT and the filled BiI_3 NT@CNT. (**c**) An enlarged image of the filled region in a. (**d**) Corresponding FFT indicating the orientation relationship between BiI_3 (003) (red circle) and CNT (002) (yellow circle).
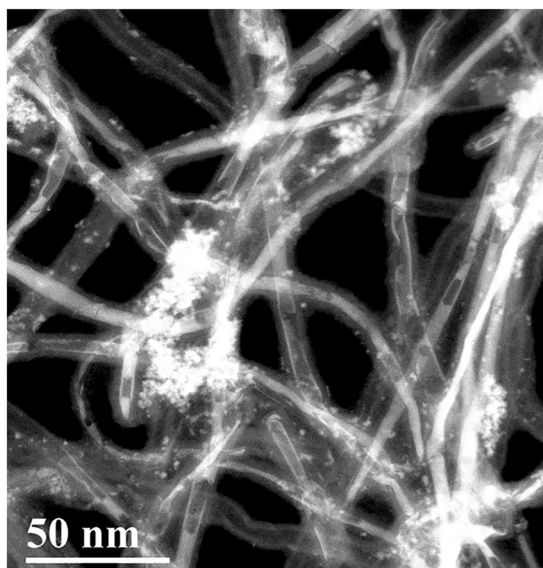

Figure 5. Low magnification image of BiI_3@CNT showing encapsulation as nanotubes, partially filled nanotubes and nanorods.

encapsulation is observed to be greater than 80%. In order to identify the MWCNT diameter regime where the formation of single walled BiI_3 nanotubes is favorable, we performed statistical analysis of the samples obtained from the host MWCNTs of different diameters. Supplementary Fig. S6 shows the inner diameter distribution of four MWCNT samples investigated. CNT 1, with a mean inner diameter of 2.31 nm resulted in exclusive formation of nanorods. CNTs with larger diameters (CNT 2, CNT 3 and CNT 4) facilitated the formation of single walled BiI_3 nanotubes along with nanorods of BiI_3. Supplementary Fig. S7 shows the frequency distribution of BiI_3 nanotubes and nanorods depending on the MWCNT diameters. A preferential formation of nanotubes at larger diameters is observed in all the latter three CNT samples. In a previous report on PbI_2@CNT, a range of diameters between 4 to 8 nm was suggested to facilitate the formation of nanotubes[3]. Herein, a host inner diameter of ~3 nm is identified as the lowest threshold for the formation of single-walled BiI_3 nanotubes and nanotubes as large as 12 nm in diameter were also observed in the CNTs. In addition, the possibility of formation of NTs and NRs of other halides of bismuth is elucidated with the example of $BiCl_3$ (Supplementary Figs S8–S10).

In order to understand the relative stability and possible modulation of electronic properties of BiI_3 in the nanotubular state, DFT calculations have been employed. Preliminary geometry optimizations of both the bulk
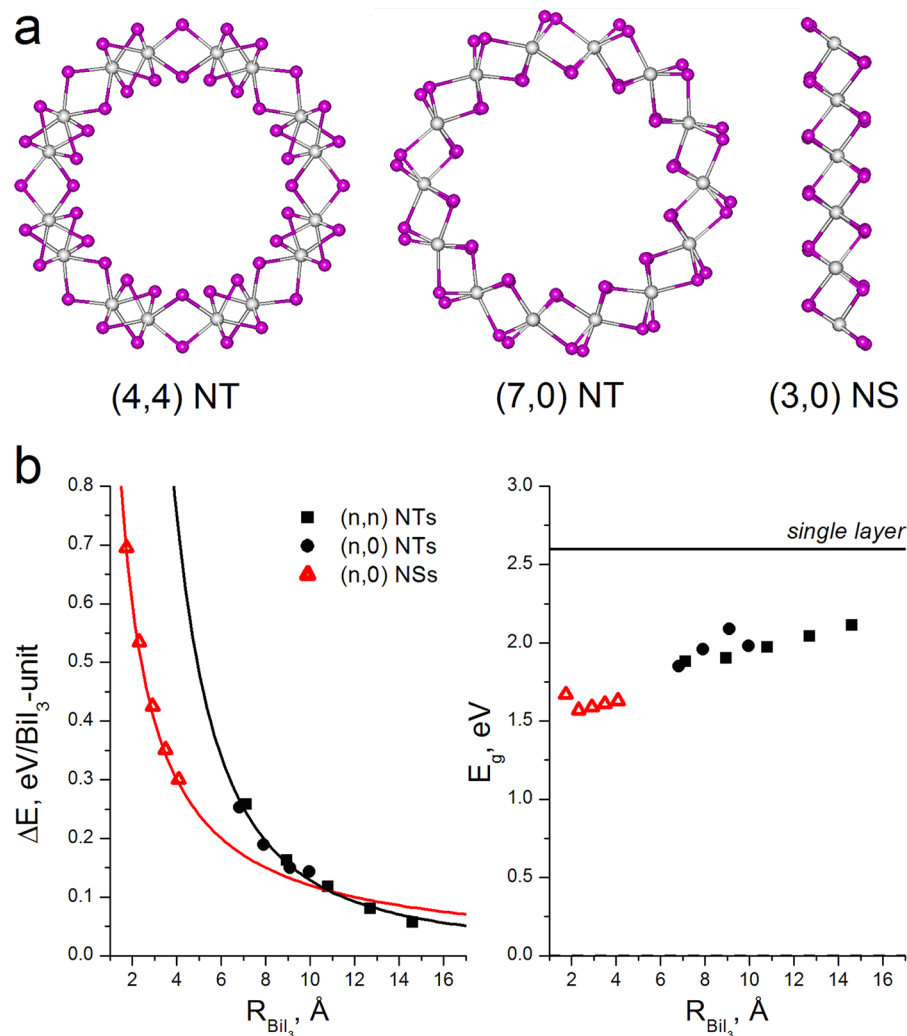
Figure 6. (**a**) Ball-and-stick models of exemplary one-dimensional single-walled BiI_3 nanostructures after geometry optimization using DFT method: *armchair* (4,4) and *zigzag* (7,0) nanotubes, *zigzag* (3,0) nanostripe (the views along main axes, Bi and I atoms are in white and violet). (**b**) Strain energies ΔE and band gaps E_g for different BiI_3 nanostructures depending on their radii (for a nanostripe the radius corresponds to the width normalized by 2π).

BiI_3 and a free-standing single sheet BiI_3 do not show evidence about a distortion of layers' hexagonal symmetry. Isolated BiI_3 layer undergoes a minor in-plane contraction, adopting the equilibrium lattice parameter $a = 7.26$ Å (for the bulk $a = 7.52$ Å).

The construction principles of BiI_3 SWNTs coincide with those for the well-known graphene-derived CNTs. The TEM images of BiI_3 SWNTs encapsulated into MWCNTs suggest that they are likely chiral and may possess even a variable chirality along the axis of bent MWCNTs. Hence, the nanotubes of two extreme chiralities have been considered: armchair (n,n) with n = 3–7 and zigzag (n,0) with n = 5–8 (Fig. 6a), which are computationally also less demanding, than chiral nanotubes. The properties of nanotubes were compared to those of BiI_3 nanostripes - as single layer nanorods - with both glide- and mirror-symmetric armchair edges: zigzag (n,0) with n = 2, 3 and chiral (n,1) with n = 1–3 (Fig. 6a). To decrease computational demands, our study of nanorods was limited only to the single-layer members. Yet, the main contribution into excessive total energy of both nanorods and nanostripes arises from the energy of dangling bonds at the edges, and a weak interlayer (mainly van der Waals) interaction may be neglected here.

Preservation of morphological integrity after geometry optimization has been observed for all BiI_3 nanostructures irrespective of the chirality type in all range of chosen indices. To trace the relative stability as a function of both the radius and the chirality of nanotubes and nanostripes, their excessive energies ΔE were defined as the energies relative to the energy of the BiI_3 monolayer. Hence, the main contribution to ΔE, for nanotubes or flat nanostripes, is due to the pure strain energy and the energy of dangling bonds at edges, respectively. The values of ΔE per BiI_3-unit are collected in Fig. 6b. The data confirm that, the main factor defining the morphological stability of cylindrical nanotubes is the radius R. Irrespective of the chirality, the DFT calculated values ΔE for
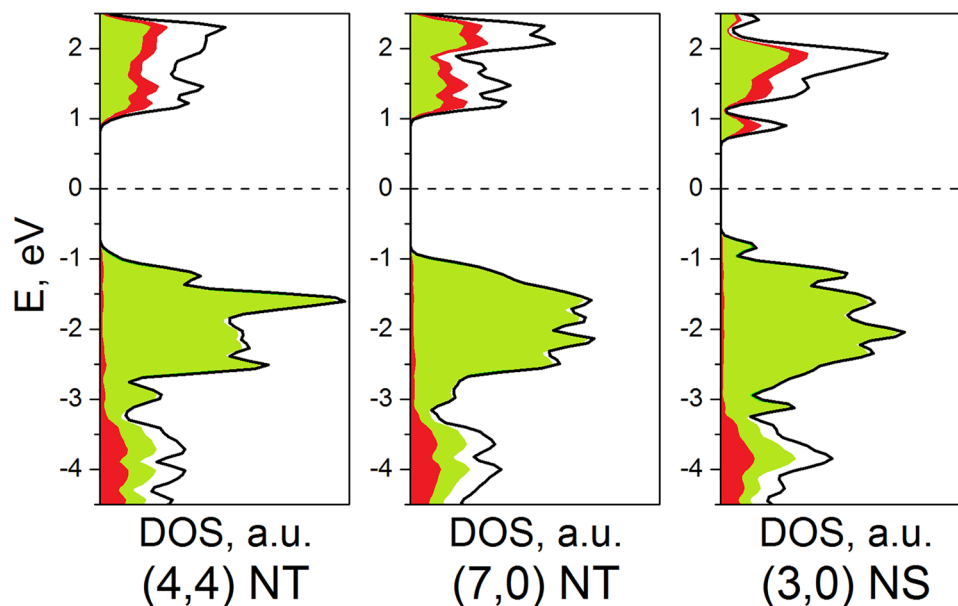
Figure 7. Densities-of-states (DOS) for exemplary one-dimensional BiI$_3$ nanostructures (Fermi level is set to 0.0 eV). Total DOS is outlined in black, valence Bi6p- and I5p-states are painted in red and green, respectively.

SWNTs can be interpolated using a single function, obeying the ~$1/R^2$ rule predicted in the framework of classical elasticity theory for a bent layer.

The proportionality factor between ΔE and $1/R^2$ for all considered BiI$_3$ nanotubes is found to be equal to 11.87 (eV·Å^2)/unit or 3.0 (eV·Å^2)/atom. This factor depends essentially on the layers' thickness and lies between the previously reported values of 0.5 (eV·Å^2)/atom and 16.1 (eV·Å^2)/atom, for SWCNT and MoS$_2$ nanotubes, respectively[29]. Noteworthy, that both carbon and MoS$_2$ nanotubes can be produced in large amounts nowadays. Therefore, our calculations reveal, the elastic strain of the BiI$_3$ layers should not be the main constraint to a future mass synthesis of the BiI$_3$ nanotubes. The lower boundary of the stability of BiI$_3$ SWNTs is predestined by the energy of dangling bonds at the edges of corresponding BiI$_3$ nanostripes as unrolled nanotubes. The values of ΔE per BiI$_3$-unit for nanostripes obey ~$1/R$ rule (Fig. 6b), which reflects a negligible dependence of the energy of dangling bonds on the width and an identical geometry reconstruction of the edges at different nanostripes. However, the most important outcome can be found in the cross-point of ΔE functions for nanostripes and nanotubes. BiI$_3$ SWNTs become thermodynamically more stable at diameters larger, than 2.2 nm. The calculated band structures and the densities of electronic states (DOS) for selected nanotubes and nanostripes of BiI$_3$ are visualized in Fig. 7 and Supplementary Fig. S11. The DOS profile and relative location of the bands observed for different single walled nanostructures can be found qualitatively similar, exhibiting also a very close similarity with those of the single layer. In accordance to the polar covalent character of the Bi-I bonding, the valence band at $-1...-3$ eV is composed of mainly I5p-states, while the valence band at $-3...-5$ eV and the bottom of conduction band are the mixtures of I5p- and Bi6p-states.

All the studied BiI$_3$ nanostructures are semiconductors likely with the direct band gaps at Γ-point, yet, with too narrow dispersions at the occupied and conduction edges of the band gaps. The band gap values do not fall below 1.5 eV and in the case of SWNTs they approach the value for the single BiI$_3$ layer 2.5 eV (Fig. 7, Supplementary Fig. S11). The latter value is found overestimated in agreement with previous theoretical study[30], since no spin-orbit coupling was accounted in our calculations of nanostructures. While the fundamental band gap of BiI$_3$ remains disputable, our calculations unveil a tendency in modulation of the band gap of enrolled BiI$_3$ layers[31], hence, the nanotubes, too. The vanishing of their fundamental band gaps at low R can be explained by a strengthened overlapping between the Bi6p- and I5p-orbitals at interior side of nanotube, yet, not manifesting itself through the localized states in the fundamental band gap, which is typical for the dangling bonds. The band gap modulation for flat BiI$_3$ nanostripes has another background. In fact, their band structure demonstrates the same fundamental band gap ~2.5 eV as that for the single layer. Yet, several states split off from both the conduction and the valence bands, leading to formal decrease of the band gap. These localized states are associated with the edge atoms of a low coordination: five-fold Bi and monodentate I atoms, respectively.

Regrettably, direct DFT calculation with correction on spin-orbit coupling is computationally too expensive for BiI$_3$ nanostructures due to the geometric and atomistic sizes of their unit cells. However, our preliminary estimations of the band gaps should contain only a systematic error and should qualitatively reproduce the trends in band gap modulations of different nanotubes and nanostripes. The folding of a planar layer into cylindrical nanotube facilitates the orbitals' overlapping at internal side of nanotube. Noteworthy, this situation is equivalent to the external pressure applied to the bulk BiI$_3$. Devidas et al. have demonstrated that at a high pressure the band gap of the bulk polymorphs of BiI$_3$ gets decreased in experiment as well as in both schemes of DFT calculations: without and with spin-orbit coupling[32].

Conclusions

In conclusion, capillary filling was employed for obtaining bismuth halides encapsulated within MWCNTs. In the case of BiI_3, we have observed single walled nanotube with hexagonal crystal structure within the MWCNT host. Such core-shell nanotubes could lead to novel fundamental properties and also applications. Diameter dependence of the nanotube formation versus nanorods were analyzed using statistics obtained from electron microscopy images. Our results show a lower threshold inner diameter of the host MWCNT of ~3 nm, which is the minimum diameter for the formation of BiI_3 single-walled nanotubes. These experimental observations agree very well with the DFT calculations which have been carried out in the present study to understand the energetics of their formation.

Methods

Synthesis and Characterization.   The encapsulation of BiI_3 and $BiCl_3$ in MWCNT was carried out by capillary filling. The bismuth halide along with CNT, vacuum sealed in a quartz ampule, was annealed in a furnace above the melting point of the halide and subsequently cooled to room temperature. The conditions for the synthesis of BiI_3@CNT and $BiCl_3$@CNT are given in Tables S1 and S2, respectively. Samples for TEM/STEM analysis were prepared on holey carbon film 300 mesh Cu grids. A FEI Titan Themis 60–300 kV electron microscope, operated at 80 kV, equipped with probe and image correctors and a monochromator, was used for TEM and STEM imaging. EDX spectra were obtained using a Super-X detector and EELS measurements were carried out on an Enfinium ER spectrometer. Crystal models were built using Crystal maker software and diffraction patterns were simulated using the Single crystal software.

Computational Details.   The DFT calculations within the Generalized Gradient Approximation after Perdew-Burke-Ernzerhof parametrization were performed using the SIESTA 4.0 package[33]. The norm-conserving Troullier–Martins pseudopotentials were used for the description of the core electrons[34], while the valence electron shells were adapted as $5s^25p^5$ for I and $6s^26p^3$ for Bi with the pseudopotential core radii corresponding to 2.24 a_B and 2.26 a_B for I5s- and I5p-states, 2.88 a_B for all Bi states. The valence orbitals were described using double zeta basis set, including polarization functions. The numerical integrations were performed using the real-space grid with the 300 Ry energy cutoff. The k-point mesh for periodic systems established after Monkhorst - Pack and a cutoff of 15 Å were employed for k-point sampling[35]. For 1D and 2D structures the lattice parameter in "non-periodic" directions was chosen as 40 Å. Both the lattice parameters and the atomic positions of a unit cell were optimized until the total residual force and a residual stress component have achieved 0.05 eV/Å and 0.1 GPa, respectively.

Data availability.   All data generated or analysed during this study are included in this published article (and its Supplementary Information files).

References

1. Višić, B., Panchakarla, L. S. & Tenne, R. Inorganic nanotubes and fullerene-like nanoparticles at the crossroads between solid-state chemistry and nanotechnology. *J. Am. Chem. Soc.* **139**, 12865–12878 (2017).
2. Nakanishi, R. *et al.* Thin single-wall BN-nanotubes formed inside carbon nanotubes. *Sci. Rep.* **3**, 1385, https://doi.org/10.1038/srep01385 (2013).
3. Cabana, L. *et al.* Synthesis of PbI_2 Single-layered inorganic nanotubes encapsulated within carbon nanotubes. *Adv. Mater.* **26**, 2016–2021 (2014).
4. Tenne, R. Recent advances in the research of inorganic nanotubes and fullerene-like nanoparticles. *Front. Phys.* **9**, 370–377 (2014).
5. Rao, C. N. R. & Govindaraj, A. In *Nanotubes and Nanowires (2)* 243–342 (The Royal Society of Chemistry, 2011).
6. Seifert, G., Köhler, T. & Tenne, R. Stability of metal chalcogenide nanotubes. *J. Phys. Chem. B* **106**, 2497–2501 (2002).
7. Brüser, V. *et al.* Single- to triple-wall WS_2 nanotubes obtained by high-power plasma ablation of WS_2 multiwall nanotubes. *Inorganics* **2**, 177–190 (2014).
8. Sandoval, S., Pach, E., Ballesteros, B. & Tobias, G. Encapsulation of two-dimensional materials inside carbon nanotubes: Towards an enhanced synthesis of single-layered metal halides. *Carbon* **123**, 129–134 (2017).
9. Ajayan, P. M. & Iijima, S. Capillarity-induced filling of carbon nanotubes. *Nature* **361**, 333–334 (1993).
10. Tsang, S. C., Harris, P. J. F. & Green, M. L. H. Thinning and opening of carbon nanotubes by oxidation using carbon dioxide. *Nature* **362**, 520–522 (1993).
11. Tsang, S. C., Chen, Y. K., Harris, P. J. F. & Green, M. L. H. A simple chemical method of opening and filling carbon nanotubes. *Nature* **372**, 159–162 (1994).
12. Dujardin, E., Ebbesen, T. W., Hiura, H. & Tanigaki, K. Capillarity and wetting of carbon nanotubes. *Science* **265**, 1850–1852 (1994).
13. Petrosko, S. H., Johnson, R., White, H. & Mirkin, C. A. Nanoreactors: Small spaces, big implications in chemistry. *J. Am. Chem. Soc.* **138**, 7443–7445 (2016).
14. Li, G. *et al.* Giant raman response to the encapsulation of sulfur in narrow diameter single-walled carbon nanotubes. *J. Am. Chem. Soc.* **138**, 40–43 (2016).
15. Fujimori, T. *et al.* Conducting linear chains of sulphur inside carbon nanotubes. *Nat Commun* **4**, 2162, https://doi.org/10.1038/ncomms3162 (2013).
16. Giusca, C. E. *et al.* Confined crystals of the smallest phase-change material. *Nano Lett.* **13**, 4020–4027 (2013).
17. Fornaro, L., Aguiar, I., Pérez Barthaburu, M. & Pereira, H. B. Synthesis of mercuric iodide and bismuth tri-iodide nanoparticles for heavy metal iodide films nucleation. *Cryst. Res. Technol.* **46**, 1317–1322 (2011).
18. Cuña, A., Aguiar, I., Gancharov, A., Pérez, M. & Fornaro, L. Correlation between growth orientation and growth temperature for bismuth tri-iodide films. *Cryst. Res. Technol.* **39**, 899–905 (2004).
19. Aguiar, I., Olivera, A., Mombrú, M., Heinkel, B. P. & Fornaro, L. Novel bismuth tri-iodide nanostructures obtained by the hydrothermal method and electron beam irradiation. *J. Cryst. Growth* **457**, 244–249 (2017).
20. Boopathi, K. M. *et al.* Solution-processable bismuth iodide nanosheets as hole transport layers for organic solar cells. *Sol.r Energy Mater. Sol. Cells* **121**, 35–41 (2014).
21. Han, H. *et al.* Defect engineering of BiI_3 single crystals: Enhanced electrical and radiation performance for room temperature gamma-ray detection. *J. Phys.Chem. C* **118**, 3244–3250 (2014).
22. Brandt, R. E. *et al.* Investigation of bismuth triiodide (BiI_3) for photovoltaic applications. *J. Phys. Chem. Lett.* **6**, 4297–4302 (2015).

23. Kreizman, R. *et al*. Synthesis of core–shell inorganic nanotubes. *Adv. Funct. Mater.* **20**, 2459–2468 (2010).
24. Li, Y. *et al*. Bismuth nanotubes: A rational low-temperature synthetic route. *J. Am. Chem. Soc.* **123**, 9904–9905 (2001).
25. Boldt, R., Kaiser, M., Köhler, D., Krumeich, F. & Ruck, M. High-yield synthesis and structure of double-walled bismuth-nanotubes. *Nano Lett.* **10**, 208–210 (2010).
26. Rasche, B., Seifert, G. & Enyashin, A. Stability and electronic properties of bismuth nanotubes. *J. Phys. Chem. C* **114**, 22092–22097 (2010).
27. Kiang, C.-h Electron irradiation induced dimensional change in bismuth filled carbon nanotubes. *Carbon* **38**, 1699–1701 (2000).
28. Deepak, F. L., Mayoral, A. & Arenal, R. E. In *Advanced Transmission Electron Microscopy: Applications to Nanomaterials*. (Springer International Publishing, 2015).
29. Tenne, R., Remškar, M., Enyashin, A. & Seifert, G. In *Carbon Nanotubes Topics in Applied Physics* (ed. Ado Jorio Gene Dresselhaus Mildred S. Dresselhaus) 635–675 (Springer, 2008).
30. Ma, F. *et al*. Single Layer Bismuth iodide: Computational exploration of structural, electrical, mechanical and optical properties. *Sci. Rep.* **5**, 17558, https://doi.org/10.1038/srep17558 (2015).
31. Podraza, N. J. *et al*. Band gap and structure of single crystal BiI_3: Resolving discrepancies in literature. *J.Appl. Phys.* **114**, 033110 (2013).
32. Devidas, T. R. *et al*. Pressure-induced structural changes and insulator-metal transition in layered bismuth triiodide, BiI_3: a combined experimental and theoretical study. *J. Physics: Condens. Matter* **26**, 275502 (2014).
33. Ordejon, P., Artacho, E. & Soler, J. M. Self-consistent order-N density-functional calculations for very large systems. *Phys. Rev. B* **53**, R10441 (1996).
34. Troullier, N. P. & Martins, J. L. Efficient pseudopotentials for plane-wave calculations. *Phys. Rev. B* **43**, 1993–2006 (1991).
35. J. Moreno, J. & Soler, J. M. Optimal meshes for integrals in real- and reciprocal-space unit cells. *Phys. Rev. B* **45**, 13891 (1992).

Author Contributions

A.E.A. prepared the samples and conducted the electron microscopy. A.N.E. carried out the DFT calculations. F.L.D. directed the entire study. All the authors discussed the results and wrote the paper.

Additional Information

Supplementary information accompanies this paper at https://doi.org/10.1038/s41598-018-28446-2.

Competing Interests: The authors declare no competing interests.

Publisher's note: Springer Nature remains neutral with regard to jurisdictional claims in published maps and institutional affiliations.